NLTT 41135: A FIELD M DWARF + BROWN DWARF ECLIPSING BINARY IN A TRIPLE SYSTEM, DISCOVERED BY THE MEARTH OBSERVATORY

JONATHAN IRWIN[1], LARS BUCHHAVE[1,5], ZACHORY K. BERTA[1], DAVID CHARBONNEAU[1], DAVID W. LATHAM[1], CHRISTOPHER J. BURKE[1], GILBERT A. ESQUERDO[1], MARK E. EVERETT[1], MATTHEW J. HOLMAN[1], PHILIP NUTZMAN[1], PERRY BERLIND[2], MICHAEL L. CALKINS[2], EMILIO E. FALCO[2], JOSHUA N. WINN[3], JOHN A. JOHNSON[4,6], AND J. ZACHARY GAZAK[4]

[1] Harvard-Smithsonian Center for Astrophysics, 60 Garden St., Cambridge, MA 02138, USA; jirwin@cfa.harvard.edu
[2] Fred Lawrence Whipple Observatory, Smithsonian Astrophysical Observatory, 670 Mount Hopkins Road, Amado, AZ 85645, USA
[3] Department of Physics, Kavli Institute for Astrophysics and Space Research, Massachusetts Institute of Technology, Cambridge, MA 02139, USA
[4] Institute for Astronomy, University of Hawaii, Honolulu, HI 96822, USA
Received 2010 February 23; accepted 2010 June 8; published 2010 July 14

ABSTRACT

We report the discovery of an eclipsing companion to NLTT 41135, a nearby M5 dwarf that was already known to have a wider, slightly more massive common proper motion companion, NLTT 41136, at 2″.4 separation. Analysis of combined-light and RV curves of the system indicates that NLTT 41135B is a $(31$–$34) \pm 3 M_{\rm Jup}$ brown dwarf (where the range depends on the unknown metallicity of the host star) on a circular orbit. The visual M dwarf pair appears to be physically bound, so the system forms a hierarchical triple, with masses approximately in the ratio 8:6:1. The eclipses are grazing, preventing an unambiguous measurement of the secondary radius, but follow-up observations of the secondary eclipse (e.g., with the *James Webb Space Telescope*) could permit measurements of the surface brightness ratio between the two objects, and thus place constraints on models of brown dwarfs.

Key words: binaries: eclipsing – brown dwarfs – stars: individual (NLTT 41135) – stars: low-mass

Online-only material: color figures and machine-readable tables

1. INTRODUCTION

The formation mechanism of brown dwarfs, star-like objects whose masses are too low to sustain hydrogen fusion in their interiors, has remained a theoretical puzzle ever since they were first detected. They pose a problem for standard star formation theories relying on gravitational collapse of molecular cloud material because their masses are substantially smaller than the typical Jeans mass in such a cloud.

Although considerable theoretical and observational effort has been expended, there is still no clear consensus on how brown dwarfs form. Popular theoretical ideas can be divided into three major sub-groups. The first relies on finding some mechanism to produce a sufficiently low-mass core ab initio, while circumventing the Jeans mass problem. This can be done, for example, by turbulent fragmentation of cloud material (e.g., Padoan & Nordlund 2004), fragmentation and subsequent collapse of molecular cloud cores (e.g., Boss 2002), or erosion of cores by ionizing radiation from nearby massive stars (e.g., Whitworth & Zinnecker 2004). The second scenario posits that brown dwarfs form as part of multiple systems (which collapse from a single large overdensity, thus circumventing the Jeans mass problem), and are then ejected before they can accrete sufficient mass to become normal hydrogen burning stars (e.g., Reipurth & Clarke 2001). Finally, disk fragmentation mechanisms (e.g., Rice et al. 2003; Stamatellos & Whitworth 2009) are proposed, by which stars and brown dwarfs form by gravitational instability. Similar mechanisms have been proposed for planet formation (e.g., Boss 2006), and Kratter et al. (2010) note that disk fragmentation in the outer regions of protoplanetary disks naturally leads to the formation of brown dwarfs.

Multiple systems offer an important clue as to the nature of the star formation process and could give an insight into the problem of brown dwarf formation. Observations indicate that while multiple systems are extremely common for solar type stars, with approximately 65% of systems found to harbor one or more components (e.g., Duquennoy & Mayor 1991), the multiplicity fraction appears to decline through M spectral types to the brown dwarf domain, with only 42% of field M dwarf systems being multiple (e.g., Fischer & Marcy 1992). The fraction could be as low as 10% for late-M and L dwarfs, although there is some disagreement in the literature regarding corrections for the effects of survey biases, particularly in binary semimajor axis (see Burgasser et al. 2007 and references therein for a review). One formation mechanism that naturally generates a low multiplicity fraction for brown dwarfs is the ejection hypothesis mentioned above (Reipurth & Clarke 2001) since it relies on dynamical interactions, which would likely disrupt most binary brown dwarf systems. However, this mechanism has difficulty explaining other observational evidence, such as the existence of disks around brown dwarfs (e.g., Jayawardhana et al. 2003), which would also be disrupted by dynamical interactions.

In addition, binary systems have long been a cornerstone in our understanding of the fundamental properties of stars because gravity provides one of the few model-independent means to precisely measure the mass of a star for comparison with other fundamental properties, thus allowing us to test stellar evolution theory. Double-lined eclipsing binaries (EBs) are particularly useful in this regard, where combined analysis of light curves and radial velocity (RV) information can determine masses and radii for both stars to very high precision (Torres et al. 2010; see also the classic review by Andersen 1991).

Results of recent dynamical mass measurements for brown dwarf binaries indicate that the there may be substantial discrepancies between the predictions of evolutionary models and the observed masses and luminosities of the objects, by factors of up to 2 or 3. There has been some debate in the literature as to the nature of these discrepancies, with the earliest example finding that the luminosities were overpredicted for a given mass (Close et al. 2005; but this may have been due to an error in the spectral type, see Close et al. 2007), whereas other studies found that they are underpredicted (Dupuy et al. 2009a), or indicate no discrepancy (e.g., Liu et al. 2008; and Dupuy et al. 2009b for an intriguing object at the L/T transition). Konopacky et al. (2010) present measurements of an unprecedentedly large sample of objects, concluding that the discrepancies are a function of spectral type, with late-M to mid-L systems having luminosities overpredicted by the theoretical models, and one T-type system having a luminosity which is underpredicted, indicating that the sense of the discrepancies may reverse moving to later spectral types. Furthermore, the evolutionary and atmospheric models may indeed be inconsistent with one another (e.g., Dupuy et al. 2009a; Konopacky et al. 2010), indicating systematic errors in one or both classes of models.

The only well-characterized double lined brown dwarf EB is perhaps even more puzzling, showing a reversal in the effective temperatures of the two objects, with the more massive brown dwarf being cooler (Stassun et al. 2006, 2007). This is thought to be due to magnetic activity in this extremely young ($\sim$1–2 Myr) system (Chabrier et al. 2007). What is clear is that even more dynamical measurements of brown dwarfs are needed to place these results on a firmer footing and to probe a wider range of parameter space.

In this work, we present the detection of an eclipsing brown dwarf orbiting the lower-mass member of a known field M dwarf visual double, NLTT 41136 and 41135, which we show are highly likely to be physically associated. The observation of eclipses constrains the orbital inclination, and thus allows the secondary mass to be ascertained through RV measurements with essentially no $\sin i$ ambiguity. The properties of the parent M dwarf can also be constrained from the eclipse measurements. Such an object represents an opportunity to constrain formation and evolutionary models of both M and brown dwarfs.

2. OBSERVATIONS AND DATA REDUCTION

2.1. MEarth Photometry

Eclipses in NLTT 41135 were initially detected from data taken during 2009 February to May (inclusive) as part of routine operation of the MEarth observatory, a system designed primarily to search for transiting super-Earth exoplanets orbiting around the nearest 2000 mid to late M dwarfs in the northern hemisphere (Nutzman & Charbonneau 2008; Irwin et al. 2009). Exposure times on each field observed by MEarth are tailored to achieve sensitivity to the same planet size for the assumed parameters of each target star, and were 151 s for the field containing NLTT 41135.

Data were reduced using the standard MEarth reduction pipeline, which is at present nearly identical to the Monitor project pipeline described in Irwin et al. (2007). We used an aperture radius of 10 pixels (7″6); note that the MEarth telescopes were operated slightly out of focus in the 2008 September–2009 July observing season to increase the number of photons that can be gathered before the saturation of the detector for our brightest targets.

This star was identified as a high-priority candidate from a box-fitting least-squares (BLS) transit search (following closely the methods of Burke et al. 2006) performed on de-trended, median filtered light curves. We used a 3 day median filter (Aigrain & Irwin 2004) to remove stellar variability, followed by a trend filtering algorithm (TFA; Kovács et al. 2005) based on searching for optimal linear combinations of comparison star light curves to best remove any systematic effects in the target light curve. The photometry indicated a period of approximately 2.8 days and a 2% eclipse depth, with no secondary eclipses visible in the MEarth data. We immediately switched to a follow-up mode after the initial detection, observing the object at the highest possible cadence (approximately 3 minutes including overheads) during the night of UT 2009 May 25 when an eclipse was predicted to occur. This was confirmed with high significance, although any measurements of the eclipse shape were severely corrupted by the target crossing the meridian during the eclipse, which necessitates a temporary halt in the observations and rotation of the telescope optics and detector system through 180° relative to the sky with our German equatorial mounts. In practice, the telescope guiding takes some time to recover after this, and photometry is corrupted during the recovery period. Therefore, while we were able to confirm the reality of the event, the MEarth data are not useful in determining the eclipse shape or physical properties of the object.

Due to the close proximity of NLTT 41135 and 41136, these stars are unresolved in the MEarth observations, and indeed are also unresolved or improperly resolved in many well-known literature sources for measurements of bright stars. It was initially not clear which member of the M dwarf pair was undergoing eclipses, so we pursued photometric (resolved light curves) and spectroscopic (RV) methods to determine the identity of the eclipsing star. The spectroscopic method gave the earliest indication that NLTT 41135 was responsible for the eclipses.

The high proper motion of the pair allows us to constrain the contribution of any additional background stars in the photometric aperture that are not co-moving with NLTT 41135 and 41136 using previous epochs of imaging. We show in Figure 1 a series of three images centered on the position of the photometric aperture used in the MEarth images. These show that there is a fainter star located approximately 7″ to the east and 1″ to the north of the blended pair at the MEarth epoch. Using the APM online sky catalog[7], this star is 4 mag fainter than the blended image of NLTT 41135 and 41136 in the POSS-1 red (E) plate, and 2.3 mag fainter in the blue (O) plate. While this star is at the edge of the MEarth photometric aperture and thus will affect the eclipse depths measured from these data, we have ensured that this star was excluded from the apertures used to analyze the follow-up data described in the subsequent sections, and its fainter magnitude and bluer color should ensure any contamination in the far-red bandpasses used in this work is negligible.

Our MEarth light curves show variations out of eclipse. These have a peak-to-peak amplitude of $\simeq$0.04 mag and rms scatter of 0.012 mag. There is no clear period, and it is not clear which member of the pair is responsible for the variations. Our photometry is corrupted somewhat by the partially resolved nature of the pair, so we regard this measurement as an upper limit to the actual variability level, noting that the absence of a

---

7 http://www.ast.cam.ac.uk/~apmcat/
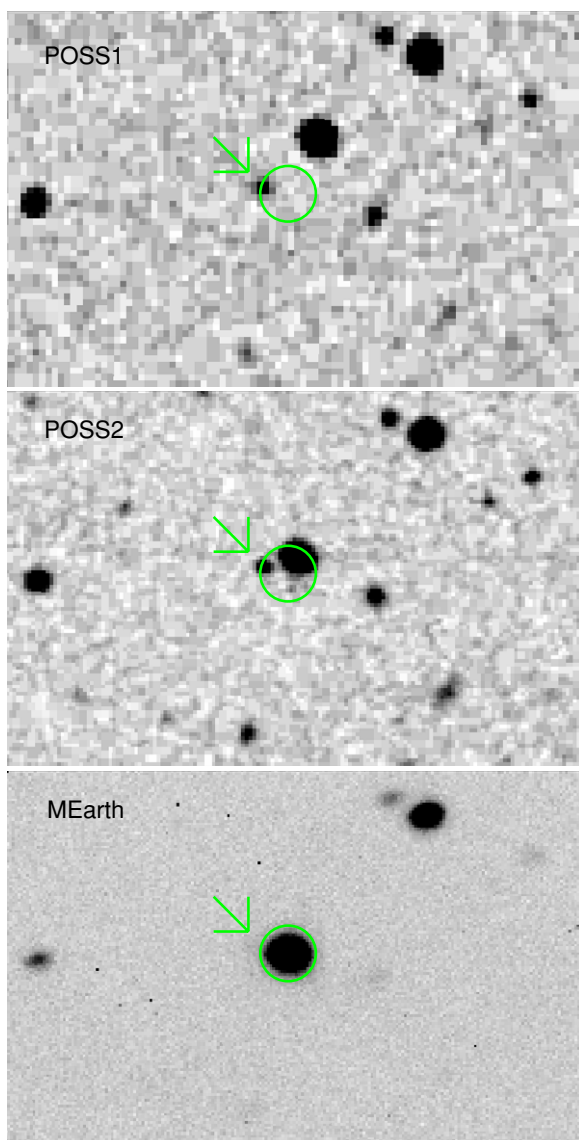
Figure 1. Images of NLTT 41135 and 41136 centered on the position as measured from the MEarth data. The circle shows the approximate position and size of the 7″.6 (radius) photometric aperture used to derive our light curves, and the arrow points to the position of the fainter star discussed in the text. Data are from the first and second epoch Palomar sky surveys as provided by the Digitized Sky Survey (DSS; top and center panels), and the MEarth master image (bottom panel). The two stars are unresolved, although elongation of the combined image is visible in the POSS-2 (center) panel. The approximate epochs of the images are 1954.4 (POSS-1), 1993.2 (POSS-2), and 2009.1 (MEarth). All three panels have the same center, scale and alignment on-sky, with north up and east to the left, covering approximately 2′.5 in the horizontal direction.

(A color version of this figure is available in the online journal.)

clear period may be indicative of some or all of the measured variation being spurious.

2.2. UH 2.2 m z-band Resolved Follow-up Photometry

In order to determine the flux ratio of the M dwarf pair, and hence the intrinsic flux decrement during eclipse, we obtained a single, resolved image of the system using the Orthogonal Parallel Transfer Imaging Camera (OPTIC; Howell et al. 2003; Tonry et al. 2005) on the University of Hawaii 2.2 m telescope, during the night of UT 2009 June 9. This instrument uses two 2048×4096 "orthogonal transfer" CCDs (e.g., Tonry et al. 1997) which allow parallel transfers of the charge through the

image area in both the *x*- and *y*-directions. The pixel scale is 0″.14/pix on the 2.2 m telescope, giving a field of view of 9′.3 × 9′.3. An exposure time of 10 s was used in good seeing conditions through the *z* filter. The Heliocentric Julian Date of mid-exposure was 2454991.910257, corresponding to an orbital phase of 0.23 (close to quadrature) for the NLTT 41135 system (see Section 2.8).

This single image was bias subtracted using the overscan region, and flat-fielded before using our standard source detection software to obtain positions and aperture photometry for both stars in the pair. We measured an angular separation of 2″.40, and a flux ratio of $l_{41136,z}/l_{41135,z} \equiv L_3 = 2.1 \pm 0.2$, where we have assumed a conservative error based on multiple measurements of the image made using different sized apertures. This quantity will later be used in the analysis of unresolved light curves of the system to extract the parameters of the eclipsing binary, NLTT 41135. In this context, it is usually referred to as "third light," and shall hereafter be labeled with the symbol L_3 for consistency with the usual nomenclature in the eclipsing binary literature.

It is important to consider the possible influence of stellar variability on the value of L_3. Using the results stated in Section 2.1, in a similar passband, the most pessimistic assumption is to assign all of the measured variation to NLTT 41135, giving a contribution to the fractional uncertainty in L_3 of 4% (rms). Our assumed uncertainty of ± 0.2 (a fractional uncertainty of 10%) in L_3 is already sufficient to account for this, and the additional contribution from variability is probably negligible.

An attempt to obtain a resolved light curve was made on the night of UT 2009 June 17. Exposure times of 25 s were used through the *z* filter. We used the orthogonal parallel transfer capability of the OPTIC detector to shift charge during the exposure in an attempt to perform a tip-tilt correction of the incoming wavefronts to improve the FWHM of the images. However, due to technical problems, this instead caused severe corruption of the point spread functions (PSFs), which limits the utility of the resulting light curve. In addition, during the eclipse the guiding lock was lost which caused a short gap in the phase coverage. Nonetheless, we were able to extract resolved photometry of the two stars by performing standard aperture photometry on the resulting images. An aperture radius of 4 pixels (0″.56) was found to give the best compromise between flux losses from the aperture and cross-contamination of the PSFs of the two stars. We used NLTT 41136 as the comparison star to extract differential photometry of NLTT 41135, which has the additional advantage of canceling much of the cross-contaminated flux between the two objects and hence providing a more accurate measurement of the true eclipse depth. This light curve is given in Table 1.

2.3. FLWO 1.2 m z-band Follow-up Photometry

Observations centered around the primary eclipse of UT 2009 June 20 were obtained using the KeplerCam instrument on the Fred Lawrence Whipple Observatory (FLWO) 1.2 m telescope. We used the standard binning 2×2 readout mode, since the pixel scale of 0″.34 per unbinned pixel significantly oversamples the typical seeing at FLWO. The resulting scale was 0″.67 per summed pixel. We used the *z* filter and an exposure time of 120 s. A total of 86 observations were taken, starting approximately 1 hr before first contact and finishing 0.5 hr after last contact to sample the out-of-eclipse portions of the light curve, thus allowing the eclipse depth to be properly measured.

Table 1
UH 2.2 m Resolved z-band Light Curve

HJD[a]	Differential z	Error[b]	Δm[c]	FWHM[d] (pix)	Air mass	x[e] (pix)	y[e] (pix)
2454999.853406	−0.0502	0.0039	−0.567	6.36	1.03609	482.569	3423.312
2454999.854022	−0.0358	0.0064	−0.474	2.95	1.03604	474.552	3421.937
2454999.854670	0.0192	0.0043	−0.371	6.02	1.03601	477.566	3419.809
2454999.855283	0.0048	0.0037	−0.088	5.88	1.03599	475.421	3421.553
2454999.855896	0.0261	0.0040	−0.103	6.32	1.03600	469.411	3419.771

Notes.

[a] Heliocentric Julian Date of mid-exposure. All HJD values reported in this paper are in the UTC time-system.

[b] Estimated using a standard CCD noise model, including contributions from Poisson noise in the stellar counts, sky noise, readout noise, and errors in the sky background estimation.

[c] Correction to the frame magnitude zero point applied by the differential photometry procedure. More negative numbers indicate greater losses. Please note that this has already been applied to the "differential z" column and is provided only for reference (e.g., distinguishing frames with large losses due to cloud).

[d] Median FWHM of the stellar images on the frame. The plate scale was $0\overset{''}{.}14$/pix.

[e] x and y pixel coordinates on the CCD image, derived using a standard intensity-weighted moments analysis.

(This table is available in its entirety in a machine-readable form in the online journal. A portion is shown here for guidance regarding its form and content.)

Table 2
FLWO 1.2 m z-band Light Curve

HJD[a]	Differential z	Error[b]	Δm[c]	FWHM[d] (pix)	Air mass	x[e] (pix)	y[e] (pix)
2455002.740052	−0.0000	0.0012	0.013	3.91	1.12786	497.620	524.552
2455002.741672	0.0025	0.0012	−0.006	4.00	1.12904	497.732	524.679
2455002.743188	0.0000	0.0013	−0.019	4.20	1.13026	497.800	524.485
2455002.744751	0.0013	0.0012	0.007	3.87	1.13162	497.716	524.532
2455002.746302	−0.0001	0.0013	0.016	3.85	1.13307	497.629	524.695

Notes.

[a] Heliocentric Julian Date of mid-exposure. All HJD values reported in this paper are in the UTC time-system.

[b] Estimated using a standard CCD noise model, including contributions from Poisson noise in the stellar counts, sky noise, readout noise and errors in the sky background estimation.

[c] Correction to the frame magnitude zero point applied by the differential photometry procedure. More negative numbers indicate greater losses. Please note that this has already been applied to the "differential z" column and is provided only for reference (e.g., distinguishing frames with large losses due to cloud).

[d] Median FWHM of the stellar images on the frame. The plate scale was $0\overset{''}{.}67$/pix.

[e] x and y pixel coordinates on the CCD image, derived using a standard intensity-weighted moments analysis.

(This table is available in its entirety in a machine-readable form in the online journal. A portion is shown here for guidance regarding its form and content.)

These photometric data were reduced using the same pipeline as described in Section 2.1. The FWHM of the stellar images was approximately $2\overset{''}{.}5$, so we used an aperture radius of 8 binned pixels, corresponding to $5\overset{''}{.}4$ on-sky, to extract aperture photometry of the combined light of NLTT 41135 and NLTT 41136, reproduced in Table 2. Our attempts at PSF fitting photometry on the images to extract individual light curves did not yield useful results.

2.4. Sloan Digital Sky Survey Photometry

Our target lies within the survey area for the Sloan Digital Sky Survey (SDSS). In Data Release 7 (DR7; Abazajian et al. 2009), the object is resolved in the SDSS images, but appears to be blended with a false galaxy detection in the band-merged catalogs, so some of the magnitudes may be unreliable. We therefore re-derive resolved magnitudes for the two stars from the reduced images.

The relevant fpC "corrected frames" were retrieved from the SDSS archive. We used the r-band image for source detection, since this had the smallest FWHM of $\simeq 2.8$ pixels. The positions derived therefrom were then used to perform aperture photometry on the g-, r- and z-band images, using

an aperture radius of 2.5 pixels ($1\overset{''}{.}0$) to avoid overlap between the apertures placed on the two components of the visual binary. The i image appears to be corrupted for NLTT 41136, so we did not attempt to derive photometry from it, and the u-band image showed very low counts for the M dwarf pair, as expected, so this was also omitted, and is likely of limited utility in any case due to a well-documented red leak issue with the SDSS u filter affecting measurements of very red targets.

The final calibrated magnitudes are given in Table 4. We estimate uncertainties in these measurements by comparing our measurements of other stars in the image with the SDSS DR7 photometry, and allowing for cross-contaminated flux between the apertures placed on our targets. The photometric errors in g are large, due to in part the greater FWHM of the stellar images in this band compared to r and z, necessitating a larger aperture correction. The orbital phase of these measurements for the NLTT 41135 system was approximately 0.34 (see Section 2.8), and the measured z-band flux ratio is 2.03, which is consistent with the value reported from the OPTIC data in Section 2.2.

Our measurements in g and z for our target stars are systematically brighter than those reported in the SDSS DR7 catalog, which we suspect to be due to de-blending of the false "galaxy"

detection from the stellar images. The images of our target do not appear to be saturated in the SDSS data.

2.5. FLWO 1.5 m TRES Spectroscopy

Spectroscopic observations of both stars were obtained using the TRES fiber-fed échelle spectrograph on the FLWO 1.5 m Tillinghast reflector. We used the medium fiber (2″.3 projected diameter), yielding a resolving power of $R \simeq 44,000$.

We obtained two epochs on each star in the visual binary close to the predicted times of the quadratures from the photometric ephemeris in order to search for large-amplitude RV variability. One-hour exposures were obtained in June 2009 over a 4 day period.

The radial velocities were extracted using a custom-built pipeline to rectify and cross correlate the spectra. This pipeline was identical to the one used for the Nordic Optical Telescope (NOT) data and will be described in the next section.

The two radial velocities of NLTT 41135 from TRES showed variations in phase with the prediction from the photometric ephemeris, giving an initial estimate of the RV semiamplitude of $K = 12.9 \pm 0.5$ km s^{-1}. We cross correlated the spectra of the two stars and subtracted the orbital motion of the low-mass companion of NLTT 41135. If the pair of stars are physically bound, this relative velocity should be constant over short (few day) timescales and close to zero. We found a velocity difference of 860 ± 130 m s^{-1} over 4 days, which is consistent with the pair being physically bound, within the errors. These results encouraged us to obtain high signal-to-noise high-resolution spectra to characterize the RV variations of NLTT 41135.

We note that NLTT 41135 shows the Hα line in emission, whereas NLTT 41136 does not, and instead there is a hint of an absorption feature at this wavelength in our low signal-to-noise spectra. This is reasonably consistent with expectation for a field-age M dwarf system given the rapid increase in the observed Hα activity fraction around M4 to M5 spectral types (e.g., West et al. 2004), but it may also be indicative of enhanced activity on NLTT 41135 due to tidal effects from the close companion causing it to rotate more rapidly.

2.6. NOT/FIES Spectroscopy

Precise radial velocities of NLTT 41135 were obtained using the fiber-fed échelle spectrograph (FIES) on the 2.5 m NOT at La Palma, Spain. We used the medium resolution fiber (1″.3 projected diameter) with a resolving power of $R \simeq 46,000$ giving a wavelength coverage of $\simeq 3600$–7400 Å. We obtained seven high-resolution, high signal-to-noise spectra of NLTT 41135 during a seven night run in August 2009.

The spectra were rectified and cross correlated using a custom built pipeline designed to provide precise radial velocities for échelle spectrographs. The procedures are described in more detail in L. Buchhave el al. (2010, in preparation) and will be described briefly below. In order to effectively remove cosmic rays, each observation was split into three separate exposures, enabling us to combine the raw images using median filtering, removing virtually all cosmic rays. We use a flat field to trace the échelle orders and to correct the pixel to pixel variations in CCD response, then extract one-dimensional spectra using the "optimal extraction" algorithm of Hewett et al. (1985; see also Horne 1986). The scattered light in the two-dimensional raw image is determined and removed by masking out the signal in the échelle orders and fitting the inter-order scattered light flux with a two-dimensional polynomial. The FIES sky

fiber was broken at the time these observations were taken, so sky subtraction could not be performed. Unfortunately, this means we are also unable to measure equivalent widths, e.g., to characterize the activity of the star.

Thorium argon (ThAr) calibration images were obtained through the science fiber before and after each stellar observation. The two calibration images are combined to form the basis for the fiducial wavelength calibration. FIES and TRES are not vacuum spectrographs and are only temperature controlled to 1/10th of a degree. Consequently, the RV errors are dominated by shifts due to pressure, humidity, and temperature variations. In order to successfully remove these large variations (>1.5 km s^{-1}), it is critical that the ThAr light travels along the same optical path as the stellar light and thus acts as an effective proxy to remove these variations. We have therefore chosen to sandwich the stellar exposure with two ThAr frames instead of using the simultaneous ThAr fiber, which may not exactly describe the induced shifts in the science fiber and can also lead to bleeding of ThAr light into the science spectrum from the strong argon lines, especially at redder wavelengths. The pairs of ThAr exposures are co-added to improve the signal-to-noise ratio (S/N), and the centers of the ThAr lines are found by fitting a Gaussian function to the line profiles and a two-dimensional fifth order Legendre polynomial is used to describe the wavelength solution.

Once the spectra have been extracted, a cross correlation is performed order by order. The spectra are interpolated to a common oversampled log wavelength scale, high and low pass filtered, and apodized. The orders are cross correlated using a Fast Fourier Transform (FFT) and the cross correlation functions (CCFs) for all the orders co-added and fit with a Gaussian function to determine the RV. For the FIES spectroscopy, 10 orders (of a total of 78) typically yielded usable cross-correlations, where the majority of the orders we did not use are in the blue and had very poor S/Ns. For TRES, 8–10 orders were used. Uncertainties were estimated by fitting Gaussians to the individual orders' cross correlation functions, and taking the error in the mean of all the orders. The template used in this procedure was constructed from the target spectra, initially determining the RVs by cross-correlating against the best signal-to-noise individual spectrum of the target, and then shifting and adding all of the spectra to make a single high signal-to-noise stacked template, and repeating the correlations against this to produce the final RVs.

The RV measurements of NLTT 41135 are reported in Table 3.

Since our RVs are measured with respect to the target itself, the zero point is arbitrary. We make a separate estimate of the systemic velocity itself (usually called γ in eclipsing binary studies, and we follow the same notation in this work) using the Hα emission lines in NLTT 41135. These were fit with Gaussian functions, and the resulting spectroscopic orbit was analyzed in the same way as described in Section 3 to determine the γ velocity and its error, reported in Table 5.

We do not see evidence for significant rotational broadening in the observed CCF s, where the formal FWHM of the cross-correlation peak was ≈ 12 km s^{-1}. This implies an FWHM of 8.5 km s^{-1} in the individual spectra as we used the target as its own cross-correlation template. Formally, given the stated resolving power, this would imply a contribution of ≈ 5 km s^{-1} from the star, although the uncertainty in this value is large and we do not believe the small difference in FWHM is significant in practice, as other sources can inflate the measured CCF

Table 3
Barycentric Radial Velocity Measurements of NLTT 41135

HJD[a]	v_b (m s^{-1})	σ_v (m s^{-1})	Seeing[c] (arcsec)
2455048.392461	22098.6	31.5	1.0
2455049.390174	−83.2	27.4	0.9
2455050.385098	6408.9	48.8	0.9
2455051.384396	21245.8	25.4	0.8
2455052.383913	−2062.3	33.4	0.7
2455053.381672	9464.6	38.2	1.1
2455054.373863	19808.2	52.7	1.8

Notes.
[a] Heliocentric Julian Date of mid-exposure. All HJD values reported in this paper are in the UTC time-system.
[b] Relative RV. The zero point is arbitrary and corresponds to the original reference spectrum (HJD 2455049.39). An estimate of the actual γ velocity is reported in the text and given in Table 5.
[c] Seeing estimates for a wavelength of 500 nm and an air mass of 1.0 from the Differential Image Motion Monitor (DIMM) operated by the Isaac Newton Group on the same site. See http://www.ing.iac.es/Astronomy/development/seeing/ for more information on this instrument.

Table 4
Summary of the Photometric and Astrometric Properties of NLTT 41135 and NLTT 41136

| Parameter	NLTT 41136	NLTT 41135
α_{2000}[a, b]	$15^h 46^m 04^s.41$	$15^h 46^m 04^s.26$
δ_{2000}[a, b]	$+04°41'31''.2$	$+04°41'30''.0$
$\mu_\alpha \cos \delta$[b]	$0''.156$ yr^{-1}	
μ_δ[b]	$-0''.284$ yr^{-1}	
g	16.261 ± 0.06	17.422 ± 0.06
r	14.927 ± 0.03	16.036 ± 0.03
z	12.374 ± 0.03	13.145 ± 0.03
Spectral type	M4.2 ± 0.5	M5.1 ± 0.5
$T_{\rm eff}$[c]	3340 ± 120 K	3230 ± 130 K
$d_{\rm phot}$	24.2 ± 11.2 pc	22.7 ± 6.8 pc

Notes.
[a] Equinox J2000.0, epoch 2000.0.
[b] From Lépine & Shara (2005). These authors measure only the combined proper motion of the pair, and not individual proper motions for the two stars. We have been unable to locate individual estimates in the literature.
[c] We assume a ±100 K systematic uncertainty in the effective temperatures.

width. Unfortunately, we lack observations of suitable slowly rotating M dwarf templates to make a robust measurement of the rotational broadening. However, the lack of a coherent, periodic modulation in the MEarth photometry (see Section 2.1) also indicates probable low rotation, where $v \sin i = 5$ km s^{-1} would imply a rotation period of $\lesssim 2.1$ days.

2.7. Summary of the Photometric and Astrometric System Properties

Table 4 summarizes the known system properties, from the literature (principally the proper motion survey of Lépine & Shara 2005 used to select the target stars for the MEarth survey) and the SDSS photometry. A source appears in the 2MASS point source catalog, but we do not report these measurements here since the photometry is flagged as having a very poor PSF fit and may therefore be unreliable. Comparing the predicted and measured J-band magnitudes indicates that the source detected in 2MASS is most likely NLTT 41136 only.
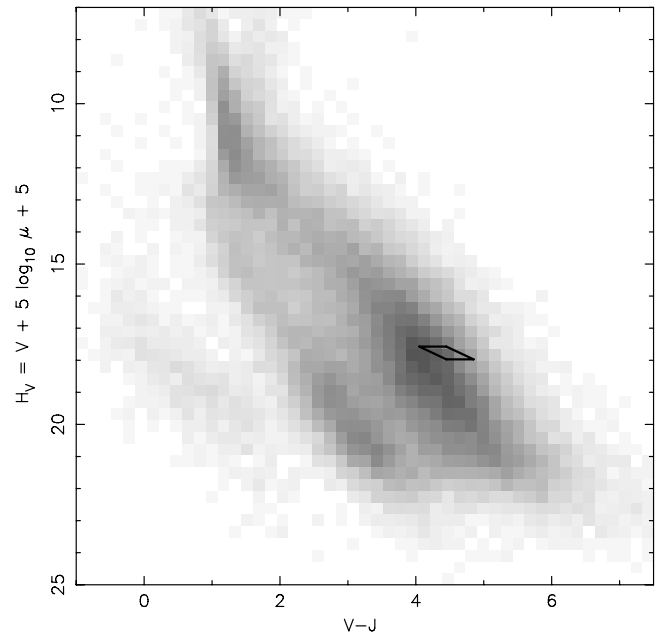
Figure 2. V vs. $V - J$ reduced proper motion diagram, reproduced from Lépine & Shara (2005), but plotted as grayscales and showing the position of NLTT 41136 by the parallelogram shaped box. See the text for a discussion of the uncertainties in determining the correct position for this object.

As a check that these objects are indeed nearby dwarfs, we show in Figure 2 the position of our source on a V versus $V - J$ reduced proper motion (hereafter RPM) diagram, reproduced from Figure 30 of Lépine & Shara (2005). Only NLTT 41136 is shown since these authors do not provide estimates of magnitudes for NLTT 41135. It is not clear if the source was resolved in the surveys used to gather their photometry (USNO-B1.0 for V and 2MASS for J), so we indicate the 0.4 mag uncertainty resulting from the possible inclusion of NLTT 41135 in either, or both, bands by the parallelogram shaped box on the diagram. Nevertheless, it appears that the position of NLTT 41136 is consistent with that expected for a nearby dwarf in RPM.

We derive photometric estimates of the spectral types for both stars using the average SDSS colors for M dwarfs of West et al. (2005), interpolating between the measured $r - z$ values in their Table 1. The derived spectral types and their uncertainties are reported in our Table 4. Note that these uncertainties are largely systematic in nature, i.e., the error in relative spectral type between the two stars is smaller than the errors we report. We have also converted the observed spectral types to effective temperature using the scale of Kenyon & Hartmann (1995). We assume a systematic uncertainty of ±100 K in the effective temperatures following Torres & Ribas (2002).

Finally, photometric estimates of the distance to each star were derived using the absolute magnitude relations from West et al. (2005), and comparing to the measured magnitudes. These distances differ by $< 1\sigma$, which, in combination with their apparent common proper motion, strongly supports our conclusion that the two stars are physically associated.

2.8. Ephemeris Determination

The small number of RV measurements gathered does not in practice place useful constraints on the ephemeris. We therefore derived this entirely from photometry, using the discovery data (after applying the filtering detailed in Section 2.1) and the times reported in Section 4 for the two well-sampled

eclipses. These were modeled with a linear ephemeris, fitting the KeplerCam light curve model from Section 4 simultaneously to the discovery data and the two eclipse timings.

We estimate the uncertainties in the ephemeris parameters using the "residual permutation" bootstrapping method (e.g., Winn et al. 2009) to account for the effects of the correlated noise (systematics) present in the MEarth data on the eclipse times. The light curve was first fit adjusting three parameters: the magnitude zero point, ephemeris zero point t_0, and period P, to compute best-fitting values for these parameters. We then proceeded to fit the model to new light curves generated by taking the original best fit and adding in cyclic permutations of the residuals from that fit. The final parameter values and their associated uncertainties were estimated using the median and central 68.3% confidence intervals of the distributions of the new parameters from these fits, over all $N - 1$ cyclic permutations of the data (where $N = 993$ is the number of data points in the MEarth light curve). In this way, the correlations in the noise are taken into account in the results.

We find that the times of mid-primary eclipse are given by $t_k = t_0 + kP$, where k is an integer, with $t_0 = 2455002.80232 \pm 0.00022$ (HJD) and $P = 2.889475 \pm 0.000025$ days.

3. RADIAL VELOCITY ANALYSIS

We fit a single Keplerian orbit model to the observed RVs using a Levenberg–Marquardt non-linear least-squares method. Since the M dwarf host star NLTT 41135 emits most of its light in the infrared and the spectral coverage of FIES ends at approximately 7400 Å, we were able to use only the reddest orders that were not affected by telluric lines. Typically, 10 orders were used in the analysis. The average internal error for the 30 minute exposures was 37 m s^{-1}. We have quadratically added a "jitter" term of 17 m s^{-1} to the velocities to yield a reduced $\chi^2 = 1.0$. We therefore estimate that the true error of the velocities is $\simeq 41$ m s^{-1}.

We fixed the mid-eclipse time and period to the values found from the photometric analysis of the light curve and assumed a circular orbit, which leaves two free parameters, namely the velocity amplitude and the γ velocity of the system. The RVs and resulting best-fitting model are shown in Figure 3, and the parameters derived therefrom are presented in Table 5. The rms variation of the residuals from the best-fit model was 39 m s^{-1}.

In order to place an upper limit on the eccentricity, we also carried out fits where the eccentricity and argument of periastron were allowed to vary (whilst enforcing consistency with the photometric ephemeris). This yielded an eccentricity of $e = 0.007 \pm 0.005$ and $K = 13.269 \pm 0.062$ km s^{-1}. We can thus constrain the eccentricity to be $e < 0.02$ with 99% confidence.

4. LIGHT CURVE ANALYSIS

For detached eclipsing binaries on circular orbits, the RV and light curve models are largely independent. Since the RV measurements show no evidence for non-zero eccentricity, we assume a circular orbit for the purposes of analyzing the light curves.
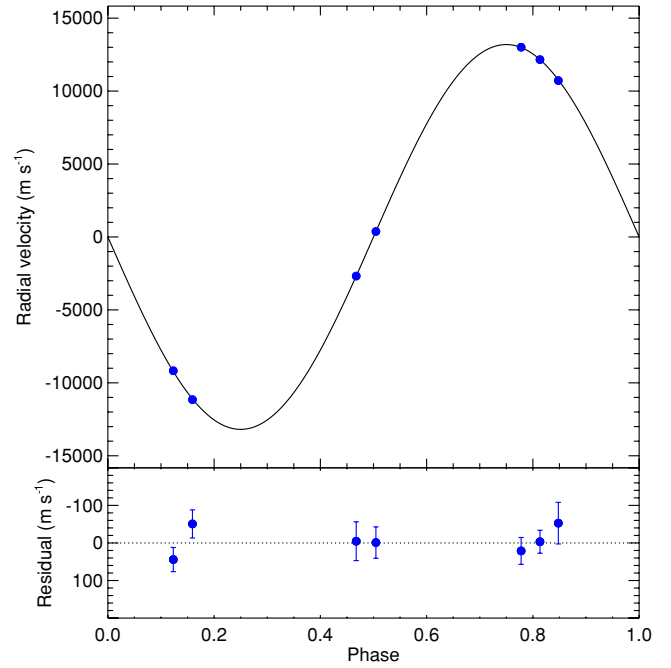
Figure 3. Upper panel: radial velocity measurements from the NOT as a function of orbital phase (measuring from 0 at the primary eclipse and in units of the orbital period; for the assumed circular orbit the secondary eclipse is at 0.5) with the best orbital fit overplotted. The γ velocity of the system has been subtracted and the fit assumes a circular orbit, fixing the ephemeris to that found by the photometry. The internal error bars are plotted, but are not visible due to their small size. Lower panel: phased residuals of the velocities after subtracting the best-fit model. The rms variation of the residuals is 39 m s^{-1}. Note that the scale of the lower panel has been expanded to better show the residuals.

(A color version of this figure is available in the online journal.)

Since we do not detect secondary eclipses, and the light from the secondary is expected to be negligible in the optical, with a predicted z-band luminosity ratio of at most $\simeq 10^{-3}$ between NLTT 41135B and NLTT 41135A for ages appropriate to an old field system (see Section 6), we assume a dark secondary for the purposes of modeling the light curve. This allows the use of simple models developed for fitting transiting exoplanet light curves.

We use the analytic transit curves of Mandel & Agol (2002) to model the KeplerCam primary eclipse light curve, modeling limb darkening with a standard quadratic law (e.g., Claret & Giménez 1990; van Hamme 1993) of the form

$$\frac{I_\lambda(\mu)}{I_\lambda(1)} = 1 - u_1(1 - \mu) - u_2(1 - \mu)^2, \quad (1)$$

where $I_\lambda(\mu)$ expresses the monochromatic intensity at wavelength λ for a point on the surface at angle θ from the normal, $\mu = \cos\theta$, and u_1 and u_2 are free parameters.

We accounted for the dilution of the eclipse depth by the presence of NLTT 41136 in the photometric apertures using the measured z-band light ratio (L_3) from Section 2.2. Since the light ratio and the light curves themselves were both observed through z filters, the error introduced by doing this should be small, and we account for its effect in the final uncertainties by assuming a conservative error on L_3.

After accounting for the known system ephemeris, the model has five free parameters: the ratio of the component radii R_2/R_1, orbital inclination i, the semimajor axis divided by the primary radius, a/R_1, and two limb darkening parameters, u_1 and u_2. In practice, we introduce three additional parameters: the

normalization (out of eclipse magnitude) z_0, a linear term in air mass $k(X - 1)$ (where X is air mass) to account for any residual differential atmospheric extinction effects, and we also allow for a timing offset Δt to account for any error in the ephemeris or deviations in the eclipse time due to orbital perturbations.

While it is usually possible (with sufficiently high-quality data) to fit for all three geometric parameters (R_2/R_1, i, and a/R_1) of a total eclipse, it is important to note that this is not possible for a grazing eclipse because the second and third contact points are no longer seen in the light curve. In the simple case with no limb darkening and a dark secondary, this can be understood as follows. For a total eclipse, it is straightforward to show that the eclipse depth is determined by the area ratio between the two objects, and is thus equal to $(R_2/R_1)^2$. The eclipse duration, and the duration (or equivalently, slope) of the partial phases (first to second contact, and third to fourth contact) are determined by i and a/R_1 (e.g., see Seager & Mallén-Ornelas 2003 for a detailed derivation). In the grazing case, although we still know the eclipse duration and the slope of the partial phases, we do not know what the level of the "bottom" of a total eclipse would be. Therefore, the parameter R_2/R_1 is essentially undetermined without external information on the other two.

Since we are primarily interested in i and a/R_1, we adopt a weak Bayesian prior on the most poorly determined parameter, R_2/R_1, and marginalize over this parameter to determine the distribution of possible values of the other two. In addition, the grazing light curve only constrains the limb darkening parameters very weakly, so we fix these at values appropriate for the z passband from Claret (2004) using the effective temperature from Table 4 and assuming $\log g = 5.0$ and solar metallicity. The theoretical uncertainty in limb darkening parameters for the z passband should be negligible compared to the intrinsic degeneracies in the modeling of the grazing eclipse for the present case.

In order to derive parameters and reliable error estimates, we adopt a variant of the popular Markov Chain Monte Carlo analysis frequently applied for transiting exoplanet systems (e.g., Tegmark 2004; Ford 2005; Winn et al. 2007). The majority of these analyses use the standard Metropolis–Hastings method (Metropolis et al. 1953; Hastings 1970) with Gibbs sampler, which has the advantage of being extremely simple to implement. We briefly describe this method here (as typically used for parameter estimation in astronomy), and then summarize the modifications made in our implementation.

Starting from an initial point in parameter space, the Metropolis–Hastings algorithm takes the most recent set of parameters and perturbs one or more parameters by a random Gaussian deviate. Gibbs sampling perturbs one parameter at a time, cycling around the parameters. If the perturbed parameter set has a lower χ^2 than its progenitor, it is accepted as a new point in the chain. If it has a larger χ^2, it is accepted with a probability $\exp(-\Delta\chi^2/2)$. If it is not accepted, the original point is repeated in the chain. The size of the perturbations are usually adjusted by manual iteration so that 20%–30% of the proposed points are accepted.

We adopt the Adaptive Metropolis algorithm of Haario et al. (2001), which dynamically updates a Gaussian proposal distribution during the simulation using the empirical covariance matrix, thus largely eliminating the need for initially tuning the proposal distributions to obtain the correct acceptance rates. This is by definition non-Markovian, but the updates are done in a way that has been shown to maintain the correct ergodicity properties of the chain.

We used a standard Levenberg–Marquardt algorithm[8] to provide the initial parameter and covariance estimates to start the chain, and used the resulting fit to re-scale the observational errors such that the reduced χ^2 was equal to unity.

For parameter estimation, we used a chain of 10^7 points, discarding the first 20% of these in order to ensure the chain had converged. The correlation lengths for all parameters were <100 points. We enforced the observed luminosity ratio between NLTT 41136 and NLTT 41135, of $L_3 = 2.1 \pm 0.2$ as discussed in Section 2.2.

As discussed earlier in this section, we have assumed a prior on the radius ratio to break the degeneracy between the parameters in the light curve model. Without any prior, the allowed values of R_2/R_1 are bounded only below (corresponding to the limiting case where the eclipse switches from being grazing to total), and are essentially unbounded above despite $R_2/R_1 \gtrsim 1$ being physically extremely unlikely.

From the radial velocities, we are left with little doubt that the secondary lies below the hydrogen burning limit (e.g., Chabrier & Baraffe 2000 and references therein) and is therefore a brown dwarf. The physics of this transition is quite well understood, and except for deuterium burning, the only source of energy for these objects is gravitational contraction. Theoretical models predict that all objects with masses in this range should have radii <0.11 $R_\odot$ after 300 Myr (Burrows et al. 1997), implying $R_2/R_1 < 0.6$. The measured radii of OGLE-TR-122b (Pont et al. 2005) and CoRoT-3b (Deleuil et al. 2008) also corroborate this theoretical argument. We can place an analogous lower limit; for example, secondary sizes smaller than the planet Neptune would require implausibly high densities at the measured secondary mass, implying $R_2/R_1 > 0.17$.

We therefore adopt a Gaussian prior, $R_2/R_1 = 0.4 \pm 0.3$, the value of which was derived by taking the predicted radius ratio from the stellar and brown dwarf models given the estimated masses of the two components, but also encapsulates the argument made in the previous paragraph. We assume a conservative error to account for the uncertainty in this estimate. An isotropic prior (i.e., uniform in $\cos i$) was assumed on the orbital inclination, and uniform priors were assumed on z_0, k, and R_1/a.

Our final parameter values and their associated uncertainties were estimated using the median and central 68.3% confidence intervals of the marginalized posterior probability distributions for each parameter, and are reported in Table 6. Figure 4 shows the best-fitting model overplotted on the light curves, and in Figure 5 we show representative two-dimensional distributions of the parameters of the model to illustrate the discussion of the degeneracies in the light curve modeling from this section. It is clear from the table that despite the inherent degeneracies in the light curve model, we do indeed obtain acceptable bounds on the inclination and a/R_1, especially recalling that the inclination appears as $\sin i$ when we come to interpret the RV measurements.

Note that the choice of a linear term in the air mass $k(X - 1)$ to represent the variations in the out-of-eclipse baseline is somewhat arbitrary. While it is reasonable to expect atmospheric extinction to affect the differential photometry at the observed level (especially given the much redder color of our target relative to the comparison stars), it is equally possible the observed "slope" is due to stellar variability. This means in practice that the depth information used in the model fits is uncertain due to the unknown contribution of stellar spots.
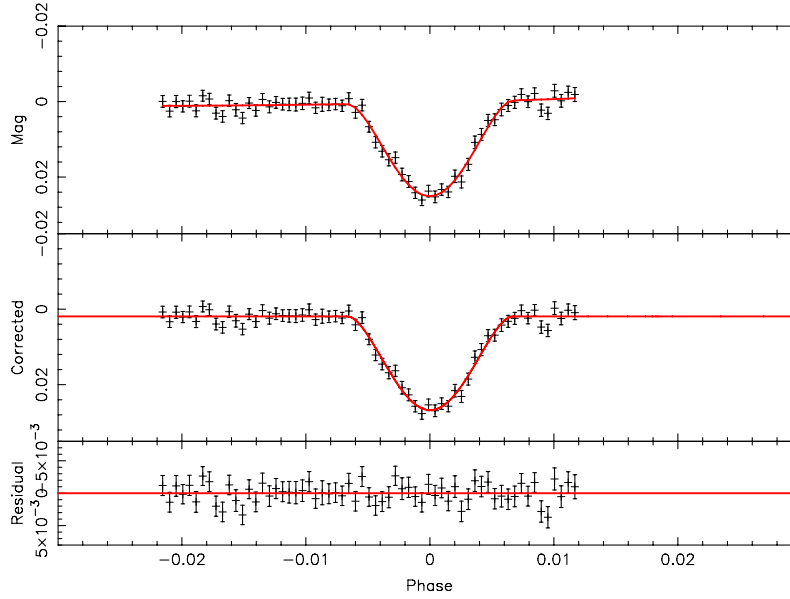
Figure 4. Top panel: phase-folded z-band KeplerCam light curve with our best-fitting light curve model overplotted. Center panel: as above, with the linear air mass term subtracted out before plotting. Bottom panel: residual after subtracting the model from the data.
(A color version of this figure is available in the online journal.)

Table 6
Parameters for the Light Curve Model of NLTT 41135

Parameter	Value
t_0 (HJD)	$2455002.80232 \pm 0.00022$
P (days)	2.889475 ± 0.000025
u_1	0.0169 (assumed)
u_2	0.6976 (assumed)
L_3	2.10 ± 0.20 (assumed)
Δt (HJD)	0.00006 ± 0.00023
k (mag/air mass)	-0.0062 ± 0.0023
i (deg)	$87.42^{+0.50}_{-0.51}$
a/R_1	$24.60^{+1.18}_{-0.93}$
R_2/R_1	$0.48^{+0.24}_{-0.15}$

Table 7
Measured Mid-Eclipse Times for NLTT 41135

HJD[a]	$(O - C)$ (s)	Cycle[b]	Instrument
2454999.91269	-13 ± 37	-1	OPTIC
2455002.80238	5 ± 20	0	KeplerCam

Notes.
[a] Heliocentric Julian Date of mid-eclipse. All HJD values reported in this paper are in the UTC time-system.
[b] Cycle number, counting from 0 at the primary eclipse at t_0, in units of the orbital period.

Assuming a sinusoidal out of eclipse modulation with the same period as the orbit, the measured value of k would correspond to a semiamplitude of $\gtrsim 0.01$ mag, or correspondingly, $\gtrsim 0.005$ mag if the period was half an orbit (e.g., ellipsoidal variation). While the MEarth photometry places limits on the actual level of out of eclipse variation (see Section 2.1), and thus on the possible phases and periods corresponding to the measured k, the unexplained out of eclipse variations seen there may indeed be consistent with the "slope" seen in the KeplerCam data.

We use the resolved light curve from Section 2.2 to verify the parameters we have derived from the KeplerCam curve, shown in Figure 6. We re-fit for the three parameters z_0, k and Δt, and assumed $L_3 = 0$ (since the light curve was resolved), but all other parameters were held fixed from the KeplerCam analysis. The fit was carried out using 3σ clipping in order to reduce the effect of the large number of photometric outliers on the fit results, and we re-scaled the observational errors such that the reduced χ^2 of the out of eclipse parts of the light curve was equal to unity. The reduced χ^2 of the full fit (including the eclipse) was 1.04.

As an additional check, we have also performed a simultaneous fit of the KeplerCam and OPTIC light curves. Separate normalization, k, and Δt values were allowed for each of the two curves, and we fit for a single set of geometric parameters (k, i, and a/R_1) and for L_3 (removing the prior used in the pre-

vious analyses and instead fitting for this parameter). We used the same clipping and re-scaling of errors carried over from the separate analyses, which should correct for any differences in the underestimation of the observational uncertainties between the two curves and produce the correct relative weights.

The values of i, R_2/R_1 and a/R_1 from this analysis differ by $\ll 1\sigma$ from those given in Table 6, providing further verification of the results. We derive $L_3 = 2.15 \pm 0.16$, which is consistent with the value assumed in the analysis of the KeplerCam light curve to $<1\sigma$. The 99% confidence interval from this fit is $1.80 < L_3 < 2.52$.

Finally, we report the mid-eclipse times from our analysis of the two well-sampled eclipses from the unresolved KeplerCam and the resolved OPTIC light curves in Table 7.

We now proceed in the next section to interpret the parameters derived from the RV and light curve modeling in terms of the physical parameters of the M dwarf NLTT 41135A and the brown dwarf NLTT 41135B.

5. PROPERTIES OF NLTT 41135A AND SYSTEM PHYSICAL PARAMETERS

Using the γ velocity from Table 5 and the measured positions, proper motions and photometric parallax from Table 4, we estimate $(U, V, W) = (-53.8 \pm 6.2, -5.0 \pm 3.0, 4.9 \pm 5.9)$ km s^{-1} using the method of Johnson & Soderblom (1987), where we adopt the definition that positive U values are away from the
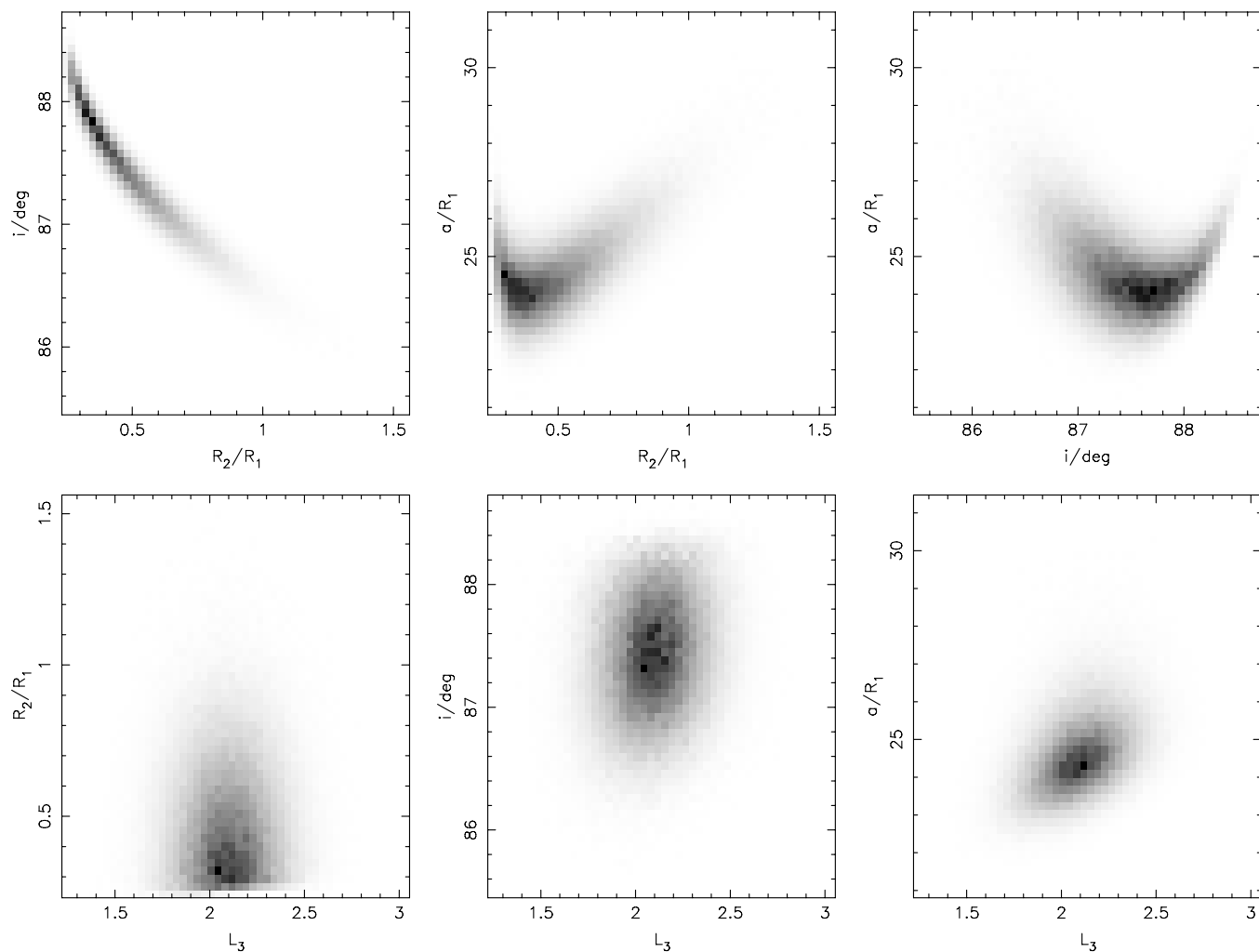
Figure 5. Two-dimensional grayscale histograms of the posterior probability density functions for selected parameter pairs from our Monte Carlo analysis. The mapping from probability density to the intensity of the grayscales was a square root function to compress the dynamic range and allow the tails of the distribution to be more readily distinguished.
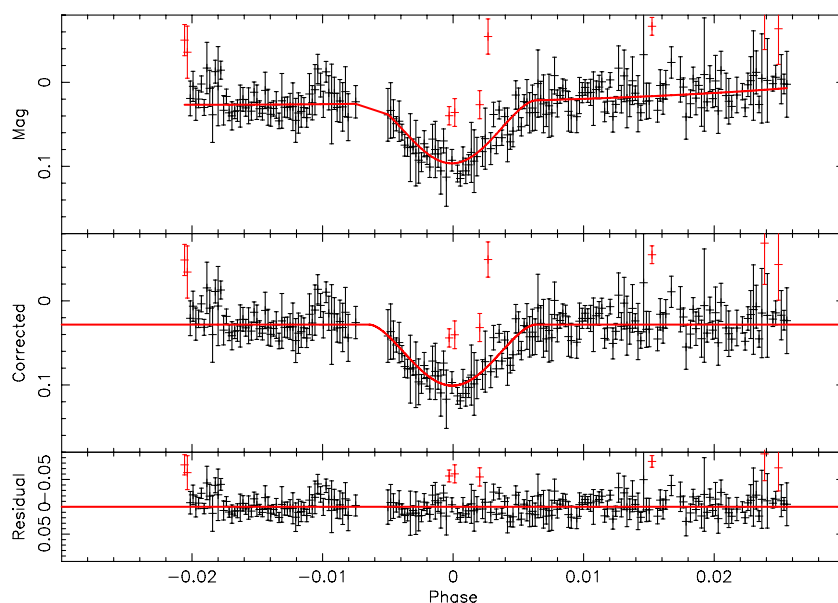
Figure 6. Phase-folded resolved z-band light curve from the OPTIC data with our best-fitting light curve model overplotted. Panels as Figure 4. Points that were excluded from the fit by our clipping procedure are colored red in the online version of the figure.

(A color version of this figure is available in the online journal.)

Galactic center. This places NLTT 41135 in the old Galactic disk population as defined by Leggett (1992). While kinematics provide relatively weak constraints on the stellar ages, these are typically a few to 10 Gyr for old disk stars, and it is thus highly likely that NLTT 41135 is older than a few Gyr.

In order to derive an estimate of the mass of NLTT 41135A, we adopt the methodology of Torres (2007), although the available information in our case is more limited since we do not have a reliable measurement of the parallax or near-infrared magnitudes.

The quantity a/R_1 from the light curve model in Section 4 provides a measurement of the mean density of the primary, $\bar{\rho}_1$ using Newton's version of Kepler's third law:

$$\left(\frac{a}{R_1}\right)^3 = \frac{G(M_1 + M_2)}{R_1^3 \Omega^2} = \frac{G(1+q)}{\Omega^2} \frac{4\pi \bar{\rho}_1}{3}, \quad (2)$$

where $\Omega = 2\pi/P$ is the angular frequency of the orbit. We explicitly note that the secondary mass is not negligible in the present case.

We use this estimate of the stellar density in conjunction with stellar evolution models to derive M_1. For this work, we adopt the tracks of Baraffe et al. (1998).

It is well established from studies of eclipsing binary stars (e.g., López-Morales 2007; Chabrier et al. 2007) that stellar evolutionary models tend to underpredict the radii of M dwarfs at a given mass. The bolometric luminosities from the same models do not seem to be seriously in error (e.g., Delfosse et al. 2000; Torres & Ribas 2002; Torres et al. 2006; Torres 2007). We therefore follow Torres (2007) and introduce a multiplicative correction factor β to the radii, while at the same time applying a factor $\beta^{-1/2}$ to the effective temperatures to conserve the bolometric luminosity. Studies of eclipsing binaries (e.g., Ribas et al. 2008) and the transiting planet host GJ 436 (Torres 2007) indicate that typical values of $\beta \simeq 1.1$.

In practice, we fit for the observed stellar density and effective temperature (from Table 4), given a fixed metallicity, and allowing the age to vary. We do not use the observed optical colors as an additional constraint because these are known to be poorly-reproduced by the models (e.g., Baraffe et al. 1998). This is thought to be the result of a missing source of molecular opacity in the NextGen model atmospheres.

The kinematic information presented in this section indicates that our target is an old, field M dwarf. We therefore explore a range of ages from 1–10 Gyr, noting that this has little effect on the derived parameters in practice, because M dwarfs in this age range evolve relatively slowly. The metallicity is also unknown, but typical values for old disk stars are [Fe/H] $\simeq -0.5$ (e.g., Leggett 1992). We derive parameters for both this value and for solar metallicity to give an idea of the likely range resulting from this source of uncertainty, which does have a significant effect on the stellar parameters.

Our derived physical parameters for NLTT 41135A, the orbital parameters, and the inferred mass of NLTT 41135B, are given in Table 8. The value of β indicates essentially no inflation of the radius of NLTT 41135A relative to the models, within the observational errors, but this is not surprising since the propagated error in the effective temperature measurement yields only a weak constraint on this parameter, with the value of 1.1 found in other studies also being reasonably consistent with the measurements.

Given the limited constraints available on the properties of NLTT 41135A, it is perhaps not surprising that the knowledge

Table 8
Derived Physical Parameters for the NLTT 41135 System

Parameter	Value	
	[Fe/H] = 0.0	[Fe/H] = −0.5
M_1 ($M_\odot$)	$0.188^{+0.026}_{-0.022}$	$0.164^{+0.021}_{-0.018}$
R_1 ($R_\odot$)	$0.210^{+0.016}_{-0.014}$	$0.201^{+0.014}_{-0.013}$
L_1 ($L_\odot$)	$0.0043^{+0.0012}_{-0.0010}$	$0.0039^{+0.0012}_{-0.0009}$
$\log g_1$	$5.062^{+0.033}_{-0.034}$	$5.072^{+0.033}_{-0.034}$
β	$1.021^{+0.057}_{-0.053}$	$1.079^{+0.059}_{-0.055}$
a ($R_\odot$)	$5.15^{+0.21}_{-0.20}$	$4.93^{+0.19}_{-0.17}$
q	$0.171^{+0.008}_{-0.008}$	$0.180^{+0.008}_{-0.008}$
M_2 ($M_{\rm Jup}$)	$33.7^{+2.8}_{-2.6}$	$30.9^{+2.4}_{-2.1}$

of the mass of the brown dwarf secondary, NLTT 41135B, is presently limited by the uncertainty in the primary mass. One of the most reliable methods to constrain single M dwarf masses in this range is to use the mass–luminosity relation, either empirical determinations such as those by Delfosse et al. (2000) or the models. We therefore suggest that the most profitable way to proceed would be to obtain an accurate trigonometric parallax, and resolved, near-infrared apparent magnitudes for NLTT 41135 and NLTT 41136. Of the available passbands, K would appear to be the logical choice, since the Delfosse et al. (2000) K-band relation is one of the best-constrained and shows the smallest scatter. This should allow the uncertainty in the primary mass to be reduced to ∼10%, and permit a test of the models of M dwarfs in addition to improving the secondary parameters. We also note that the passband-integrated luminosities of M dwarfs can be used to estimate the metallicity (e.g., Johnson & Apps 2009).

Since NLTT 41135 is a member of a presumed visual binary system, ultimately it may be possible to measure its dynamical mass from the orbit of the visual binary. This would allow a model-independent radius to be derived for NLTT 41135A, permitting a direct test of M dwarf evolution models, and would also provide a model-independent dynamical mass for NLTT 41135B. We discuss this possibility in Section 7.

6. PROSPECTS FOR CONSTRAINING BROWN DWARF EVOLUTION MODELS

While we estimate the mass of NLTT 41135B to 10%–15% (limited by the uncertain metallicity and accuracy of determination of the mass of the M dwarf host), the lack of a secondary eclipse and the detection of only one object in the spectrum mean that this is the only parameter we can presently determine.

The most straightforward approach to obtaining a second fundamental parameter for the brown dwarf is to attempt to detect a secondary eclipse. The ratio of the primary to secondary eclipse depths in a given passband is approximately the ratio of central surface brightnesses of the two objects, $J = L_2 R_1^2 / L_1 R_2^2$, where all these quantities are measured for the specific passband in question. The division by the squared radius ratio makes this a more favorable prospect than direct detection of light from the secondary, e.g., in a spectrum, and many successful detections of shallow secondary eclipses have been achieved for exoplanet systems, especially in the mid-infrared using the *Spitzer Space Telescope* (e.g., Charbonneau et al. 2005; Deming et al. 2005, 2006).

Table 9 gives the predicted luminosity ratios, surface brightness ratios, and secondary eclipse depths assuming the value of

Table 9
Predicted luminosity Ratios, Surface Brightness Ratios, and Secondary Eclipse Depths for NLTT 41135 with $A_g = 0.0$.

Age	T_2 (K)	Band	L_2/L_1	J	d_2[a] (%)
1 Gyr	1067	z	8.60×10^{-4}	3.94×10^{-3}	0.03
		J	3.51×10^{-3}	1.61×10^{-2}	0.12
		H	1.97×10^{-3}	9.04×10^{-3}	0.068
		K	1.59×10^{-3}	7.29×10^{-3}	0.055
		L'	1.04×10^{-2}	4.76×10^{-2}	0.36
		M	1.73×10^{-2}	7.95×10^{-2}	0.6
5 Gyr	643	z	1.17×10^{-4}	6.24×10^{-4}	0.0047
		J	1.84×10^{-4}	9.81×10^{-4}	0.0074
		H	1.09×10^{-4}	5.82×10^{-4}	0.0044
		K	2.04×10^{-5}	1.09×10^{-4}	0.00082
		L'	1.18×10^{-3}	6.31×10^{-3}	0.047
		M	4.26×10^{-3}	2.27×10^{-2}	0.17
10 Gyr	533	z	4.64×10^{-5}	2.61×10^{-4}	0.002
		J	5.19×10^{-5}	2.92×10^{-4}	0.0022
		H	3.14×10^{-5}	1.77×10^{-4}	0.0013
		K	2.15×10^{-6}	1.21×10^{-5}	9.1×10^{-5}
		L'	4.76×10^{-4}	2.68×10^{-3}	0.02
		M	2.31×10^{-3}	1.30×10^{-2}	0.097

Note. [a] Predicted secondary eclipse depth. We have assumed a primary eclipse depth of 7.5% based on the light curves shown in Section 4.

Table 10
Predicted Luminosity Ratios, Surface Brightness Ratios, and Secondary Eclipse Depths for NLTT 41135 with $A_g = 1.0$

Age	T_2 (K)	Band	L_2/L_1	J	d_2[a] (%)
1 Gyr	1067	z	1.22×10^{-3}	5.59×10^{-3}	0.042
		J	3.87×10^{-3}	1.78×10^{-2}	0.13
		H	2.33×10^{-3}	1.07×10^{-2}	0.08
		K	1.95×10^{-3}	8.95×10^{-3}	0.067
		L'	1.07×10^{-2}	4.92×10^{-2}	0.37
		M	1.77×10^{-2}	8.11×10^{-2}	0.61
5 Gyr	643	z	4.27×10^{-4}	2.28×10^{-3}	0.017
		J	4.94×10^{-4}	2.63×10^{-3}	0.02
		H	4.19×10^{-4}	2.23×10^{-3}	0.017
		K	3.30×10^{-4}	1.76×10^{-3}	0.013
		L'	1.49×10^{-3}	7.96×10^{-3}	0.06
		M	4.57×10^{-3}	2.44×10^{-2}	0.18
10 Gyr	533	z	3.40×10^{-4}	1.91×10^{-3}	0.014
		J	3.45×10^{-4}	1.94×10^{-3}	0.015
		H	3.25×10^{-4}	1.83×10^{-3}	0.014
		K	2.96×10^{-4}	1.66×10^{-3}	0.012
		L'	7.69×10^{-4}	4.33×10^{-3}	0.032
		M	2.60×10^{-3}	1.46×10^{-2}	0.11

Note. [a] Predicted secondary eclipse depth. We have assumed a primary eclipse depth of 7.5% based on the light curves shown in Section 4.

M_2 from Table 8 and using brown dwarf evolution models to predict the surface brightness of NLTT 41135B in near-infrared bandpasses. We use the COND models of Baraffe et al. (2003) for the secondary, and the NEXTGEN models discussed in Section 5 for the primary. We do not compute predictions for bandpasses bluer than z due to known problems with both sets of models, as mentioned earlier (see also Baraffe et al. 2003 for discussion of problems with the I-band magnitudes in the COND models), but the predicted eclipse depths are even shallower at these wavelengths due to the rapidly declining flux from the brown dwarf, so detection here seems unlikely. Three representative ages, 1, 5, and 10 Gyr, are shown in the table, with the kinematic evidence discussed in Section 5 favoring the old end of this age range.

For the purposes of these calculations, we have neglected stellar insolation. The zero albedo equilibrium temperature for NLTT 41135B is approximately 460 K, so it is likely that we underestimate the surface brightnesses, especially at the two oldest ages where insolation will represent a significant contribution to the brown dwarf energy budget.

It is also important to consider the validity of the assumption of no "reflected light" from the brown dwarf, since although its temperature is predicted to be very low, the radius should be only $\simeq 1/2$–$1/3$ that of the primary. For brown dwarfs with effective temperatures $\lesssim 1300$ K, complete gravitational settling of any dust grains should occur (e.g., Allard et al. 2001), which is the physics assumed by the COND models we have used, and should give low albedo, since the atmosphere consists mostly of absorbing species. We compute an additional set of predictions (shown in Table 10) assuming an (unrealistically large) value for the geometric albedo (A_g) equal to unity to illustrate an maximum size of this effect[9], which are reproduced in Table 10. Comparing the results in the two tables indicates that reflection should have only a very minor effect on our predictions for the

bandpasses where the secondary eclipse is most likely to be observable.

It is clear from the tables that the best prospects for detection of the secondary eclipse lie at the longest wavelengths (L' and M), and will likely require space-based observations in order to obtain adequate precision. J and to some extent H show more favorable eclipse depths than K due to the familiar blueward shift of the $J - K$ and $H - K$ colors for T dwarfs resulting from H_2 and CH_4 absorption features.

Assuming the M band to be a reasonable proxy for the longest-wavelength (4.5 μm) *Warm Spitzer* channel, this eclipse might be detectable, although it is likely that *Spitzer*'s poor angular resolution would result in the images of NLTT 41135 and 41136 being blended, thus diluting the eclipse depths by a factor of $\simeq 3$. Whilst the eclipses should still be detectable for the youngest ages we have considered, this might become extremely challenging at the more likely age of ~ 10 Gyr. Due to the rapid decline in the J band as a function of age, a similar statement applies for the prospects of detection using near-infrared instruments aboard the *Hubble Space Telescope*.

With the *James Webb Space Telescope*, the secondary eclipse detection should be straightforward, and the predicted angular resolution is sufficient to resolve the M dwarf pair even out to the mid-infrared.

It is interesting to speculate that if the secondary eclipse was total (which we stress is very unlikely given the essentially circular orbit and grazing geometry of the primary eclipse), this would yield the bandpass-integrated luminosity of the brown dwarf directly from the eclipse depth, and would break the degeneracy inherent in the modeling of the grazing eclipses in conjunction with the RV, yielding also the radii of both components.

Finally, we note that it may be possible to derive a relatively crude constraint on the radius of the brown dwarf even in the most likely case where both eclipses are grazing. Recall from Section 4 that we assumed a prior on the system radius ratio in order to determine a/R_1. However, if we knew the radius

---

[9] Upper limits from observations of secondary eclipses and phase curves in the optical for Hot Jupiter exoplanets, which are thought to have similar atmospheric constituents, indicate that $A_g \lesssim 0.1$ in the visible (e.g., Rowe et al. 2008).

of the M dwarf, a/R_1 would be already completely determined and could be fixed in the model, allowing us to instead constrain R_2/R_1. This could be done by measuring the angular diameter of NLTT 41135, in conjunction with a parallax and a K-band magnitude measurement to determine its mass. Due to the remaining strong degeneracies between R_2/R_1 and i, it is unlikely that this measurement would yield R_2/R_1 to any better than ± 0.1 (see Figure 5).

7. THE NLTT 41135/41136 VISUAL BINARY SYSTEM

Using the Baraffe et al. (1998) models, we estimate a mass ratio of $\simeq 0.8$ for the M dwarf visual pair from the effective temperatures in Table 4 (assuming [Fe/H] =-0.5, 5 Gyr age and the value of β from Table 8). Assuming the mass of NLTT 41135 from Table 8, this implies the mass of NLTT 41136 is approximately 0.21 $M_\odot$, and the total system mass is therefore $M_{\rm tot} \simeq 0.37\ M_\odot$. The angular separation of 2″40 corresponds to a projected physical separation of 55 AU at a 23 pc distance. Given this information, we can estimate a minimum orbital period of 680 yr using Newton's version of Kepler's third law.

Given the long orbital period, it will be challenging to measure the parameters of the astrometric orbit unless its orientation or eccentricity are extremely favorable, although the motion of the components relative to their presumed common proper motion could be as large as a few tens of milliarcseconds per year especially if the orbit is viewed face-on. The maximum RV difference between the pair corresponding to this period is 2.4 km s^{-1} (assuming an edge-on orbit), which is reasonably consistent with our measurements from the TRES spectroscopy (see Section 2.5) provided the measurements were taken at less than the maximum separation or the orbit is not edge-on.

8. DISCUSSION

We have reported the discovery of a hierarchical triple system containing two M dwarfs and a brown dwarf orbiting the less massive of the pair in an eclipsing system. The masses of the components are approximately in the ratio 8:6:1.

The existence of this object poses a challenge to theories of brown dwarf formation. The configuration of the system strongly resembles a scaled-down (in mass) version of a relatively common configuration for solar-type stars. The mass ratio of only 6:1 for the eclipsing binary component of the system would seem to be difficult to produce by disk fragmentation, because it would require an extraordinarily massive disk surrounding the forming M dwarf core.

Given this difficulty it seems likely that this object may have formed in the same manner as its higher-mass analogs: directly from gravitational collapse of an overdensity in a molecular cloud. It is interesting to postulate that if many such systems are made by the star formation process, there will be some that are dynamically unstable, and may eject one or more of their components. As proposed in the ejection hypothesis of brown dwarf formation (Reipurth & Clarke 2001), this may offer a mechanism to produce single brown dwarfs, although as discussed in Section 1, evidence such as the existence of single brown dwarfs with disks argues against this being the only mechanism for brown dwarf formation.

It is interesting to compare the secondary of the present system with the secondary of the CoRoT-3 system, a 22 $M_{\rm Jup}$ brown dwarf orbiting an F3V star (Deleuil et al. 2008). The brown dwarfs in the two systems have similar masses, and their orbital periods differ by only 50%, yet CoRoT-3b orbits a star of

luminosity 10^3 times greater than does NLTT 41135B, and thus experiences a 500 times greater (bolometric) stellar insolation. This means that while the energy budget of NLTT 41135B is most likely dominated by internal energy sources, CoRoT-3b will be dominated by insolation. It would thus be extremely interesting to compare the observed physical properties of these objects to obtain insights into brown dwarf physics, for example, the efficiency of re-distribution of energy from the day-side to the night-side of CoRoT-3b, as has been done for extrasolar planets (e.g., Knutson et al. 2007). We also note that these objects may have formed through different mechanisms, since the mass ratio for the CoRoT-3 system of $q = 0.015$ (an order of magnitude lower than for NLTT 41135) may be difficult to produce via conventional mechanisms thought to be responsible for binary star formation.

NLTT 41135B is also of comparable mass to the secondary in the double-lined brown dwarf EB 2MASS J05352184−0546085 (Stassun et al. 2006, 2007), although it is of much older age and orbits a main sequence star. Nonetheless, these objects are probably quite close to being evolutionary analogues of one another, and both have an energy budget most likely dominated by internal energy sources.

The present system provides a dynamical mass for a field brown dwarf, and offers the potential to allow models of brown dwarf evolution to be tested at extremely old ages, where dynamical constraints are scarce. In order to test the theory, we must attempt to determine or constrain the system age, in addition to measuring another fundamental property of the brown dwarf. The most accessible measurement is the secondary eclipse, which in conjunction with the primary eclipse yields a measurement of the central surface brightness ratio of the two components from the ratio of the eclipse depths.

Finally, we note that a major limitation in the determination of the brown dwarf mass and M dwarf parameters is the uncertainty in the mass of NLTT 41135A. We suggest that the best prospect for improvement would be to obtain an accurate trigonometric parallax for this object, in conjunction with resolved near-infrared apparent magnitude measurements (preferably in K band). This should yield an estimate for the metallicity, and thus the primary mass to $\sim 10\%$, giving an improved solution for the eclipsing binary to more tightly constrain models of low-mass stars and brown dwarfs.

REFERENCES

Abazajian, K. N., et al. 2009, ApJS, 182, 543
Aigrain, S., & Irwin, M. 2004, MNRAS, 350, 331
Allard, F., Hauschildt, P. H., Alexander, D. R., Tamanai, A., & Schweitzer, A. 2001, ApJ, 556, 357
Andersen, J. 1991, A&AR, 3, 91
Baraffe, I., Chabrier, G., Allard, F., & Hauschildt, P. H. 1998, A&A, 337, 403
Baraffe, I., Chabrier, G., Barman, T., Allard, F., & Hauschildt, P. H. 2003, A&A, 402, 701
Boss, A. P. 2002, ApJ, 568, 743
Boss, A. P. 2006, ApJ, 643, 501
Burgasser, A. J., Reid, I. N., Siegler, N., Close, L., Allen, P., Lowrance, P., & Gizis, J. 2007, in Protostars and Planets V, ed. B. Reipurth, D. Jewitt, & K. Keil (Tucson, AZ: Univ. of Arizona Press), 427
Burke, C. J., Gaudi, B. S., DePoy, D. L., & Pogge, R. W. 2006, AJ, 132, 210
Burrows, A., et al. 1997, ApJ, 491, 856

Chabrier, G., & Baraffe, I. 2000, ARA&A, 38, 337
Chabrier, G., Gallardo, J., & Baraffe, I. 2007, A&A, 472, 17
Charbonneau, D., et al. 2005, ApJ, 626, 523
Claret, A. 2004, A&A, 428, 1001
Claret, A., & Gimenez, A. 1990, A&A, 230, 412
Close, L. M., Thatte, N., Nielsen, E. L., Abuter, R., Clarke, F., & Tecza, M. 2007, ApJ, 665, 736
Close, L. M., et al. 2005, Nature, 433, 286
Deleuil, M., et al. 2008, A&A, 491, 889
Delfosse, X., Forveille, T., Ségransan, D., Beuzit, J.-L., Udry, S., Perrier, C., & Mayor, M. 2000, A&A, 364, 217
Deming, D., Harrington, J., Seager, S., & Richardson, L. J. 2006, ApJ, 644, 560
Deming, D., Seager, S., Richardson, L. J., & Harrington, J. 2005, Nature, 434, 740
Dupuy, T. J., Liu, M. C., & Ireland, M. J. 2009a, ApJ, 692, 729
Dupuy, T. J., Liu, M. C., & Ireland, M. J. 2009b, ApJ, 699, 168
Duquennoy, A., & Mayor, M. 1991, A&A, 248, 485
Fischer, D. A., & Marcy, G. W. 1992, ApJ, 396, 178
Ford, E. B. 2005, AJ, 129, 1706
Haario, H., Saksman, E., & Tamminen, J. 2001, Bernoulli, 2001, 7, 223
Hastings, W. K. 1970, Biometrika, 57, 97
Hewett, P. C., Irwin, M. J., Bunclark, P., Bridgeland, M. T., Kibblewhite, E. J., He, X. T., & Smith, M. G. 1985, MNRAS, 213, 971
Horne, K. 1986, PASP, 98, 609
Howell, S. B., Everett, M. E., Tonry, J. L., Pickles, A., & Dain, C. 2003, PASP, 115, 1340
Irwin, J., Charbonneau, D., Nutzman, P., & Falco, E. 2009, in IAU Symp. 253, Transiting Planets, ed. F. Pont, D. Sasselov, & M. Holman (Cambridge: Cambridge Univ. Press), 37
Irwin, J., Irwin, M., Aigrain, S., Hodgkin, S., Hebb, L., & Moraux, E. 2007, MNRAS, 375, 1449
Jayawardhana, R., Ardila, D. R., Stelzer, B., & Haisch, K. E. Jr. 2003, AJ, 126, 1515
Johnson, D. R. H., & Soderblom, D. R. 1987, AJ, 93, 864
Johnson, J. A., & Apps, K. 2009, ApJ, 699, 933
Kenyon, S. J., & Hartmann, L. 1995, ApJS, 101, 117
Knutson, H. A., et al. 2007, Nature, 447, 183
Konopacky, Q. M., Ghez, A. M., Barman, T. S., Rice, E. L., Bailey, J. I. iii, White, R. J., McLean, I. S., & Duchene, G. 2010, ApJ, 711, 1087
Kovács, G., Bakos, G., & Noyes, R. W. 2005, MNRAS, 356, 557
Kratter, K. M., Murray-Clay, R. A., & Youdin, A. N. 2010, ApJ, 710, 1375
Leggett, S. K. 1992, ApJS, 82, 351
Lépine, S., & Shara, P. 2005, AJ, 129, 1483
Liu, M. C., Dupuy, T. J., & Ireland, M. J. 2008, ApJ, 689, 436
López-Morales, M. 2007, ApJ, 660, 732
Mandel, K., & Agol, E. 2002, ApJ, 580, L171
Metropolis, N., Rosenbluth, A. W., Rosenbluth, M. N., Teller, A. H., & Teller, E. 1953, J. Chem. Phys., 21, 1087
Nutzman, P., & Charbonneau, D. 2008, PASP, 120, 317
Padoan, P., & Nordlund, Å. 2004, ApJ, 617, 559
Pont, F., Melo, C. H. F., Bouchy, F., Udry, S., Queloz, D., Mayor, M., & Santos, N. C. 2005, A&A, 433, 21
Reipurth, B., & Clarke, C. 2001, AJ, 122, 432
Ribas, I., Morales, J. C., Jordi, C., Baraffe, I., Chabrier, G., & Gallardo, J. 2008, Mem. Soc. Astron. Italiana, 79, 562
Rice, W. K. M., Armitage, P. J., Bonnell, I. A., Bate, M. R., Jeffers, S. V., & Vine, S. G. 2003, MNRAS, 346, 36
Rowe, J. F., et al. 2008, ApJ, 689, 1345
Seager, S., & Mallén-Ornelas, G. 2003, ApJ, 585, 1038
Stamatellos, D., & Whitworth, A. P. 2009, MNRAS, 392, 413
Stassun, K. G., Mathieu, R. D., & Valenti, J. A. 2006, Nature, 440, 311
Stassun, K. G., Mathieu, R. D., & Valenti, J. A. 2007, ApJ, 664, 1154
Tegmark, M., et al. 2004, Phys. Rev. D, 69, 103501
Tonry, J., Burke, B. E., & Schechter, P. L. 1997, PASP, 109, 1154
Tonry, J. L., Howell, S. B., Everett, M. E., Rodney, S. A., Willman, M., & VanOutryve, C. 2005, PASP, 117, 281
Torres, G. 2007, ApJ, 671, 65
Torres, G., Andersen, J., & Giménez, A. 2010, A&ARv, 18, 67
Torres, G., Lacy, C. H., Marschall, L. A., Sheets, H. A., & Mader, J. A. 2006, ApJ, 640, 1018
Torres, G., & Ribas, I. 2002, ApJ, 567, 1140
van Hamme, W. 1993, AJ, 106, 2096
West, A. A., Walkowicz, L. M., & Hawley, S. L. 2005, PASP, 117, 706
West, A. A., et al. 2004, AJ, 128, 426
Winn, J. N., Holman, M. J., & Roussanova, A. 2007, ApJ, 657, 1098
Winn, J. N., et al. 2009, ApJ, 693, 794
Whitworth, A. P., & Zinnecker, H. 2004, A&A, 427, 299